# Modeling Optical Materials at the Single Scatterer Level: The Transition from Homogeneous to Heterogeneous Materials

*Daniel Werdehausen,\* Xavier Garcia Santiago, Sven Burger, Isabelle Staude, Thomas Pertsch, Carsten Rockstuhl, and Manuel Decker*

Materials that contain distinct scatterers, for example, nanoparticles, with sizes exceeding 100 nm scatter light heavily and are heterogeneous. In contrast, the atomic or molecular scatterers in conventional optical materials form a homogeneous distribution on the scale of the wavelength. In this paper, the transition between homogeneous and heterogeneous materials is investigated. To this end, a procedure is introduced that allows for retrieving reliable refractive index values from full wave optical numerical simulations of the underlying multibody scattering problem. Using this procedure, it is shown that the concept of an effective refractive index breaks down on multiple levels as a material transitions out of the homogeneous regime. These findings allow for quantifying how novel dispersion-engineered nanocomposites for bulk optical applications must be designed and show that Maxwell–Garnett-type effective medium theories are accurate tools for the design of nanocomposites. The procedure can be readily generalized to other types of scatterers, including atoms and molecules and hence guide the design of different kinds of novel materials.

## 1. From Individual Scatterers to a Refractive Index

The use of refractive indices to describe the propagation of light in ordinary matter is one of the cornerstones of optics.[1–3] It is a powerful concept that reduces a highly complex multibody scattering problem to a single measure.[4–7] In fact, a scalar refractive index fully quantifies a material's optical response as long as it is made from microscopic scatterers whose magnetic response is negligible and which are arranged in an isotropic and homogeneous fashion . This fully holds for conventional optical materials, for example, glasses, in which the scatterers are polarizable atoms or molecules. Such materials are hence within the homogeneous regime. On the other hand, we also have a good understanding of materials that contain large scatterers, for example, nanoparticles, with sizes in the order of 100 nm.[8–15] Such materials scatter light heavily and are therefore in the heterogeneous regime. But the transition between the homogeneous and heterogenous regimes that occurs for significantly smaller scatterers has not yet been investigated in depth. To illustrate this transition, **Figure 1** visualizes how drastically the properties of a material depend on the size of its scatterers. In fact, the transition between the homogeneous and heterogeneous regimes is not only a fundamental research issue, it also has immense practical relevance for nanocomposites, which could serve as powerful next-generation

D. Werdehausen, Dr. M. Decker
Corporate Research & Technology
Carl Zeiss AG
Carl Zeiss Promenade 10, 07745 Jena, Germany
E-mail: Daniel.Werdehausen@zeiss.com

D. Werdehausen, Prof. I. Staude, Prof. T. Pertsch
Institute of Applied Physics
Abbe Center of Photonics
Friedrich Schiller University Jena
Albert-Einstein-Str. 15, 07745 Jena, Germany

X. G. Santiago, Dr. S. Burger
JCMwave GmbH
Bolivarallee 22, 14050 Berlin, Germany

X. G. Santiago, Dr. S. Burger
Zuse Institute Berlin
Takustr. 7, 14195 Berlin, Germany

X. G. Santiago, Prof. C. Rockstuhl
Institut für Nanotechnology
Karlsruher Institut für Technologie
PO-Box 3640, 76021 Karlsruhe, Germany

Prof. I. Staude
Institute for Solid State Physics
Friedrich Schiller University Jena
Max-Wien-Platz 1, 07743 Jena, Germany

Prof. T. Pertsch
Fraunhofer Institute for Applied Optics and Precision Engineering
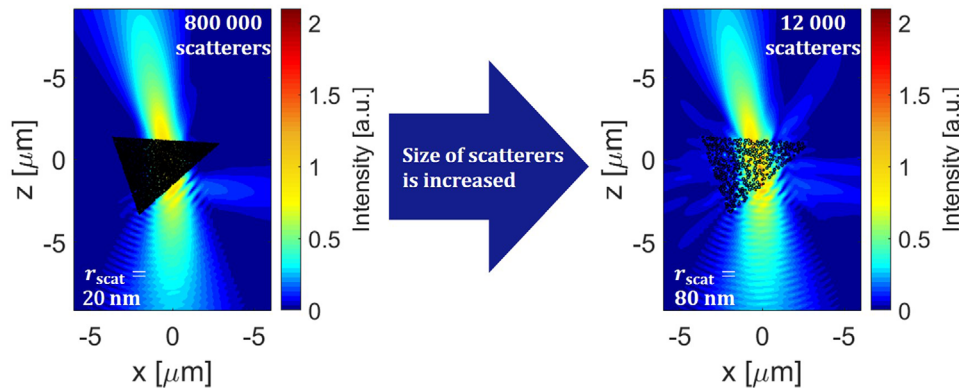Albert-Einstein-Str. 7, 07745 Jena, Germany

Prof. C. Rockstuhl
Institut für Theoretische Festkörperphysik
Karlsruher Institut für Technologie
Wolfgang-Gaede-Str. 1, 76131 Karlsruhe, Germany

Prof. T. Pertsch, Prof. C. Rockstuhl
Max Planck School of Photonics
Germany

**Figure 1.** 2D cross sections of 3D spatial intensity distributions as obtained from full wave optical T-matrix simulations. The cross sections visualize the propagation of a beam of light through a distribution of nanospheres (microscopic scatterers) that are arranged as a 3D prism with a base length and height in the $y$-direction of 6 μm. The nanospheres are made of $ZrO_2$ and are placed in air as the surrounding medium at a volume fraction of $f = 30\%$. The incident beam has a wavelength of $\lambda_0 = 0.8$ μm, a focus diameter of $\omega_{beam} = 2\lambda_0 = 1.6$ μm, and propagates in the positive $z$-direction. For the smaller nanosphere radius ($r_{scat} = 20$ nm) well-defined reflected and transmitted beams are observed, whereas for the larger radius ($r_{scat} = 80$ nm) the beams are distorted. This visualizes that optical materials become increasingly heterogeneous with increasing scatterer sizes.

optical materials.[16–21] Since nanocomposites contain distinct nanoscopic scatterers, they are also ideal prototype systems to investigate optical materials in general. This is because atoms or molecules can be treated on equal footing as nanoscopic scatterers, if their optical response is obtained from quantum mechanical simulations and captured in the notion of scattering theory.[22]

However, gaining insight into the full complexity of large-scale multibody scattering problems is a major challenge. On the one hand, effective medium theories (EMTs), which are analytical approximations that make the connection between a material's individual scatterers and its refractive index,[4,23] can never fully account for the complexity the problem.[24,25] On the other hand, experimentally controlling particle distributions that are composed of hundreds of thousands of scatterers is an immense challenge. Therefore, we still have a limited understanding of light propagation in materials at the threshold between the homogeneous and heterogeneous regimes. Full wave optical simulations are ideally suited to capture the full complexity and evaluate the applicability of EMTs. But entering the regime in which a distribution of scatterers acts as a bulk optical medium requires simulating the propagation of light through hundreds of thousands of scatterers (Figure 1). Until recently,[26] such simulations were impossible because of their high demands on computational power and memory. For these reasons, a systematic and quantitative analysis of the transition between homogeneous and heterogeneous materials has so far remained elusive.

In this paper, we use large-scale numerical simulations to investigate the transition from homogeneous to heterogeneous materials. We focus on artificial optical materials that contain dielectric nanospheres with radii between 4 and 80 nm and volume fractions of up to $f = 30\%$. Such materials recently came in the focus of attention as they enable the independent control over the magnitude and the dispersion of the refractive index.[19,27] To elucidate the properties of these artificial materials across the transition from homogeneous to heterogeneous materials and, at the same time, investigate the breakdown of the concept of an effective refractive index, we here rely on a setting in which we simulate reflection and transmission from a slab of such

materials. This allows us to use the reflected, the transmitted, or both amplitude coefficients to retrieve the material's effective refractive index and evaluate the applicability of the EMTs using these different measures. Our present paper marks the advent of a new era, in which numerical methods can be used to simulate optical materials at a single-scatterer level. We show that this enables us to obtain a deeper understanding of optical materials and guide the design of novel materials.
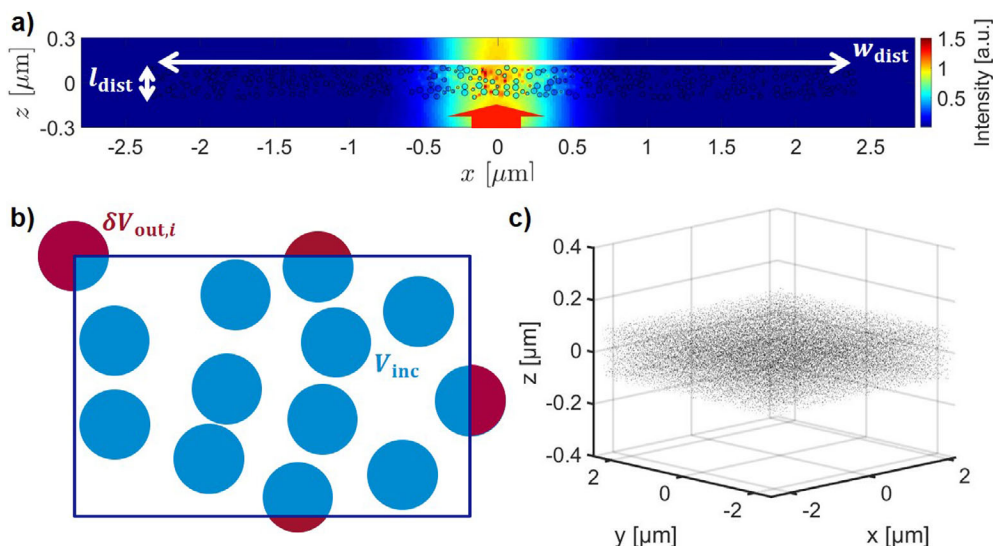
## 2. Analytical Modeling of Optical Materials

In this section, we briefly introduce the analytical approximations that make the connection between a material's microscopic structure and its refractive index. We use these expressions as a benchmark and investigate their validity compared to full wave optical simulations in detail in Section 5. The Clausius–Mossoti (CM) equation provides an analytical expression that connects a material's (effective) permittivities ($\epsilon_{eff}$) to the electric dipole polarizability ($\alpha_{scat}$) and number density ($C$) of the scatterers that make up the material.[23,28] For a fixed wavelength ($\lambda$), the CM equation reads

$$\epsilon_{eff} = \epsilon_h \frac{1 + \frac{2}{3} C \pi \alpha_{scat}}{1 - \frac{2}{3} C \pi \alpha_{scat}} \tag{1}$$

where $\epsilon_h$ is the permittivity of the homogeneous matrix that surrounds the scatterers. In the following, we focus on nanocomposites that contain distinct scatterers with a spherical shape, because methods that allow for a high-volume production mostly yield close to spherical shapes. However, this does not limit the generality of our approach because both nanoparticles with other symmetries as well as atomic and molecular scatterers can be captured within the same framework.[8,22,29–35] For spherical nanoparticles with a radius of $r_{scat}$, the electric dipole polarizability can be determined using Mie theory[36]:

$$\alpha_{scat}^{Mie} = i \frac{6 r_{scat}^3}{x^3} a_1 \tag{2}$$

**ADVANCED**
**SCIENCE NEWS**
www.advancedsciencenews.com

**ADVANCED**
**THEORY AND**
**SIMULATIONS**
www.advtheorysimul.com

**Figure 2.** a) Procedure used for determining the effective refractive index: The scatterers (nanospheres) are distributed randomly, but not-overlapping, into a box with a quadratic footprint in the $x$/$y$-plane (width $w_{dist}$) and a length in the $z$-direction of $l_{dist}$. The nanosphere distribution is then illuminated with a focused beam of light propagating in the positive $z$-direction. From the full wave optical simulations, the reflection and transmission coefficients in the normal directions are determined to retrieve the distributions' effective refractive indices. b) Procedure used for placing the scatterers: The nanospheres' center must be within the box. The total partial volume outside of the box ($\delta V_{out}$) is calculated and an additional nanosphere is placed into the box every time $\Delta V_{out}$ exceeds the volume of one nanosphere ($V_{scat}$). c) Exemplary 3D nanosphere distribution with $r_{scat} = 30$ nm.

where $a_1$ is the lowest order (electric dipole) Mie coefficient and $x = \pi \sqrt{\epsilon_h} \frac{2r_{scat}}{\lambda}$ is the size parameter.[2,37] By substituting this expression into Equation (1), the composite material's effective refractive index can be readily obtained from $n_{eff} = \sqrt{\epsilon_{eff}}$. This is the basis of the so-called Maxwell–Garnett–Mie effective medium theory (EMT), which can be used to readily estimate a nanocomposite's effective refractive index.[17] However, the CM equation, on which the EMT is based, relies on two key simplifying assumptions: First, it treats each scatterer as an electric dipole scatterer with a dipole moment of $\vec{p} = \alpha_{scat} \vec{E}_{loc}$. Second, it assumes that the local field at the scatterers' positions ($\vec{E}_{loc}$) is, on average, equal to the external field ($\langle \vec{E}_{loc} \rangle = \vec{E}_{ext}$).[23] Within these assumptions, the CM equation fully accounts for multiple scattering, that is, dipole–dipole interactions.[25] But the second assumption is only valid in two cases: 1) for perfectly random spatial particle distributions or 2) for distributions in which the particles are located on a primitive cubic lattice. Here, we focus on nanocomposites in which the particles are randomly distributed. However, in reality, impenetrable particles with a finite volume can never reach a perfectly random distribution.[25] Furthermore, the CM equation cannot account for statistical variances in the spatial particle distributions. Therefore, analytic expressions, like the CM equation, are always approximations and full wave optical simulations are required to capture the full complexity of the multibody scattering problem.

## 3. Numerical Modeling of Optical Materials

In this section, we introduce our approach for retrieving a material's refractive index from numerical simulations of the microscopic multibody scattering problem. As aforementioned, we

here focus on nanocomposites, but outline how our method can be applied to other types of scatterers.

### 3.1. Generation of 3D Particle Distributions

As the initial step of our procedure, we generate a 3D particle distribution by placing the nanospheres into a box with a quadratic footprint in the $x$/$y$ plane (width $w_{dist}$) and a length of $l_{dist}$ in the $z$-direction (**Figure 2**a). For generating these distributions, we first fix the volume fraction ($f = \frac{4}{3} C \pi r_{scat}^3$) and the nanospheres' radius at the desired values. From the volume of the box ($V_{dist} = w_{dist}^2 l_{dist}$) and an individual nanospheres volume ($V_{scat}$), we then calculate the initial number of nanospheres ($N_0$) that are required to achieve the desired volume fraction ($N_0 = f \frac{V_{dist}}{V_{scat}}$). Subsequently, we randomly place the corresponding number of nanospheres into the box such that no overlap between the particles occurs. In doing so, we allow the nanospheres to overlap with the boxes' boundaries and only require the nanospheres' centers to be inside the box (see visualization in Figure 2b). If a part of a nanosphere's volume is located outside the box, we calculate the corresponding partial volume ($\delta V_{out,i}$) using the analytical expressions from.[38] Every time the sum of the partial volumes that are located outside of the box ($\Delta V_{out} = \sum_i \delta V_{out,i}$) exceeds the volume of one nanosphere, we then place one additional nanosphere into the box. The total number of particles hence is $N_{tot} = N_0 + \lfloor \frac{\Delta V_{out}}{V_{scat}} \rfloor$, where $\lfloor \rfloor$ corresponds to the floor operator. In the Supporting Information, we show that this procedure is indispensable for obtaining well-defined volume fractions within the box and hence reliable values for the effective refractive index. An exemplary 3D view of particle distribution that we generated using this procedure is depicted in Figure 2c. Note that our procedure can be readily applied to other types of scatterers, if

**ADVANCED
SCIENCE NEWS**

www.advancedsciencenews.com

**ADVANCED
THEORY AND
SIMULATIONS**

www.advtheorysimul.com

the scatterers' partial volumes outside the box are obtained from other techniques, for example, Monte Carlo methods.[39,40]

### 3.2. Full Wave Optical Simulations

To determine the effective refractive indices of a given scatterer distribution, we illuminate each distribution with a focused beam of light (Figure 2a). We model this beam as a superposition of plane waves with a Gaussian amplitude distribution. For all data presented in this paper, we use a wavelength of $\lambda_0 = 0.8$ μm and focus the beam down to a diameter of $\omega_{\text{beam}} = \lambda_0 = 0.8$ μm (Figure 2a). We then perform a full wave optical simulation using the toolbox CELES, which combines the T-matrix method with the parallel computing capabilities of modern GPUs.[26] In all simulations, we include not only the dipole, but also the quadrupole responses of the nanospheres to ensure that we account for all higher order effects. Throughout this paper, we use $ZrO_2$ as the nanospheres' material, because its high refractive index and transparency in the visible spectral range make it a perfect prototype system for high refractive index dielectric materials.[41] As the host material we use PMMA, which is one of the most widely used optical polymers.[42] Furthermore, we focus on volume fractions below $f = 30\%$, which is the range that is commonly used in experimental works[43–49] and allows for an independent control over the magnitude and dispersion of the effective refractive index.[16]

### 3.3. Retrieval Procedure

After the numerical simulations, we decompose the resulting fields into plane waves. This allows us to determine the complex reflection ($r$) and transmission ($t$) coefficients of the distribution of scatterers. Since we here investigate random distributions, which are consequently isotropic, we determine these coefficients only for the plane waves propagating in the forward (+z) and backward (−z) directions ($k_x = k_y = 0$). Based on this data, we then use three different equations to obtain the effective refractive index. First, we use the reflection and transmission coefficients for a slab with a finite thickness:

$$r = r_{12} + \frac{t_{12}t_{21}r_{21}\phi^2}{1 - \phi^2 r_{21}^2} \quad \text{and} \quad t = t_{12}t_{21}\frac{\phi}{1 - \phi^2 r_{21}^2}, \quad (3)$$

where the reflection and transmission coefficients of the individual interfaces ($r_{ij}$ and $t_{ij}$ with $i,j \in \{1,2\}$) can be obtained from the Fresnel equations:

$$r_{12} = \frac{n_h - n_{\text{eff}}^i}{n_h + n_{\text{eff}}^i}, \qquad t_{12} = \frac{2n_h}{n_h + n_{\text{eff}}^i},$$

$$r_{21} = \frac{n_{\text{eff}}^i - n_h}{n_h + n_{\text{eff}}^i}, \quad \text{and} \quad t_{21} = \frac{2n_{\text{eff}}^i}{n_h + n_{\text{eff}}^i} \quad (4)$$

where $n_h$ is the refractive index of the surrounding medium and $n_{\text{eff}}^i$ with $i \in \{\text{trans, ref}\}$ is the effective refractive index that we determine from the transmitted ($t$) and reflected ($r$) components, respectively. Finally, the phase $\phi$ follows from

$\phi = \exp(2i\pi n_{\text{eff}}^i l_{\text{slab}}\lambda^{-1})$, where $l_{\text{slab}}$ is the slab's thickness. These expressions allow us to determine $n_{\text{eff}}^i$ independently in transmission ($i = $ trans) and reflection ($i = $ ref) by numerically inverting Equation (3). To this end, we used the requirement that the scatterer distributions' effective refractive indices must be between the ones of the host and the nanospheres' materials (real ($n_h$) ≤ real ($n_{\text{eff}}$) ≤ real ($n_{\text{scat}}$)) to constrain the numerical inversion. Furthermore, we used the prediction from the EMT as the initial value for the numerical inversion to ensure that the numerical inversion readily converges to the correct solution. In addition, in the form given in Equation (4), the Fresnel equations are only valid if the scatterers' magnetic dipole response is negligible. As a benchmark, we therefore also use an expression that relies on both $r$ and $t$ to determine $n_{\text{eff}}$ and is valid even for non-unity permeabilities in the Supporting Information. Since this equation was originally derived for photonic-crystal-type metamaterials,[50,51] we refer to the values obtained from this expression as $n_{\text{eff}}^{\text{meta}}$.
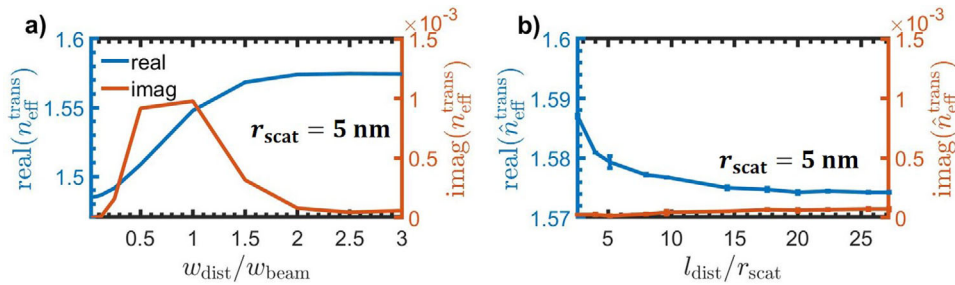
Finally, for each set of the macroscopic parameters $f$, $w_{\text{dist}}$, $l_{\text{dist}}$, and $r_{\text{scat}}$, we perform simulations for multiple random distributions to determine the influence of statistical fluctuations on the effective refractive index. A given particle distribution hence is a microstate within an ensemble that is defined by the macroscopic parameters. We refer to a set of values that we obtain for different microstates within an ensemble as $\{n_{\text{eff}}^i\}$ with $i \in \{\text{trans, ref, meta}\}$. For a given ensemble, we then determine the ensemble average $\hat{n}_{\text{eff}}^i = \text{mean}(\{n_{\text{eff}}^i\})$ and its fluctuations $\Delta n_{\text{eff}}^i = \sigma(\{n_{\text{eff}}^i\})$, where $\sigma$ denotes the standard deviation. Depending on the magnitude of the fluctuations, we investigate between 4 and 32 different microstates.

## 4. The Homogeneous Regime: Bulk Optical Media

In this section, we show that our approach allows us to enter the regime in which the distribution of scatterers acts as a homogeneous, bulk optical medium. Based on the finding that we can enter the homogeneous regime, we then investigate the breakdown of the concept of an effective refractive index that occurs with increasing scatterer size in Section 5. Since the bulk regime is reached if the particle distributions are large enough for their effective refractive index to become independent of dimensions, we first investigate the convergence with increasing box sizes ($w_{\text{dist}}$ and $l_{\text{dist}}$). For this analysis, we use a small particle radius of merely $r_{\text{scat}} = 5$ nm to ensure that the nanospheres, in good approximation, act as ideal point dipole scatterers.[17] For the sake of simplicity, we initially only consider the effective refractive index obtained from transmission ($\hat{n}_{\text{eff}}^{\text{trans}}$). Below and in the Supporting Information, we investigate the differences between $n_{\text{eff}}^{\text{trans}}$, $n_{\text{eff}}^{\text{ref}}$, $n_{\text{eff}}^{\text{meta}}$ and the EMT in detail.

**Figure 3**a depicts the real and imaginary parts of $n_{\text{eff}}^{\text{trans}}$ as functions of the distributions' widths ($w_{\text{dist}}$) for a radius of $r_{\text{scat}} = 5$ nm. For this series of simulations, we first generated a particle distribution with the maximum width ($w_{\text{dist}} = 3\omega_{\text{beam}} = 2.4$ μm) and then cropped this distribution to achieve smaller widths. Moreover, we fixed the distribution's length at $l_{\text{dist}} = 20r_{\text{scat}}$. The corresponding data in Figure 3a show that both the real and imaginary parts converge to well-defined values for widths larger than $w_{\text{dist}} = 2.5\omega_{\text{beam}}$. In the Supporting Information, we

**ADVANCED
SCIENCE NEWS**
www.advancedsciencenews.com

**ADVANCED
THEORY AND
SIMULATIONS**
www.advtheorysimul.com

**Figure 3.** Convergence of the effective refractive index obtained in transmission ($\hat{n}_{eff}^{trans}$) with a) increasing width ($\frac{w_{dist}}{\omega_{beam}}$) and b) increasing length ($\frac{l_{dist}}{r_{scat}}$) of the box that contains the nanospheres' centers. For both (a) and (b), a nanosphere radius of $r_{scat} = 5$ nm and a volume fraction of $f = 15\%$ were used. The data in (a) were obtained by first generating the particle distribution with the maximum width ($w_{dist} = 3\omega_{beam}$) and then cropping this distribution. For (b), different distributions were generated and the depicted data corresponds to the mean values, whereas the error bars denote the standard deviations. For (a), $l_{dist}$ was fixed at $l_{dist} = 20r_{scat}$. For (b), the width was fixed at $w_{dist} = 3\omega_{beam}$ with $\omega_{beam} = \lambda_0 = 0.8$ μm.

demonstrate that such a convergence is no longer achieved if the beam width is increased significantly. This shows that the use of a beam width ($\omega_{beam}$) that is much smaller than the distribution's width ($w_{dist}$) is essential for retrieving reliable values for the effective refractive indices. In this context, we note that, because of the finite size of the scatterer distribution in the transverse direction, there is a coupling between the different plane wave components that make up the focused beam. This holds true even if the scatterer distribution acts as a perfectly homogeneous material. Our finding that $\omega_{beam}$ must be sufficiently small compared to $w_{dist}$ hence demonstrates that this coupling is essential to retrieve reliable effective indices for samples of finite size. In fact, in the real world, the sizes of samples are always finite. Therefore, this finding highlights that the coupling between the plane wave components is also essential in experimental settings. We discuss this fundamental mechanism in more detail in the Supporting Information. In addition, to demonstrate that convergence is not only achieved with increasing $w_{dist}$, Figure 3 demonstrates that $\hat{n}_{eff}^{trans}$ also converges with increasing lengths around $l_{dist} = 20r_{scat}$. In the Supporting Information, we show that convergence is achieved at this length for a wide range of radii. This demonstrates that our approach indeed allows for modeling optical materials in bulk regime, in which the distribution's size does not play a role. In addition, the finding that the imaginary part of the effective refractive index almost vanishes at sufficiently large widths, demonstrates that the distribution of scatterers essentially acts as a homogeneous lossless optical medium. The number of scatterers that were required to reach this regime is in the order of 200 000. Finally, note that the particle sizes investigated here are only one order of magnitude larger than basic two-atom molecules.[52] Since molecular scatterers can be modeled within the same framework,[22] this highlights that our approach will soon allow for modeling conventional optical bulk materials at the molecular level. Note that, as opposed to our approach of modeling materials in the bulk regime, the conventional method of numerically validating a homogenization procedure only involves comparing the extinction, scattering, and absorption cross sections of a scatterer distribution that is composed of a small number of scatterers with that of the homogenized medium.[25] In fact, only little work has been done using approaches similar to ours. Commonly, these works either relied on supercells or monolayers of randomly arranged
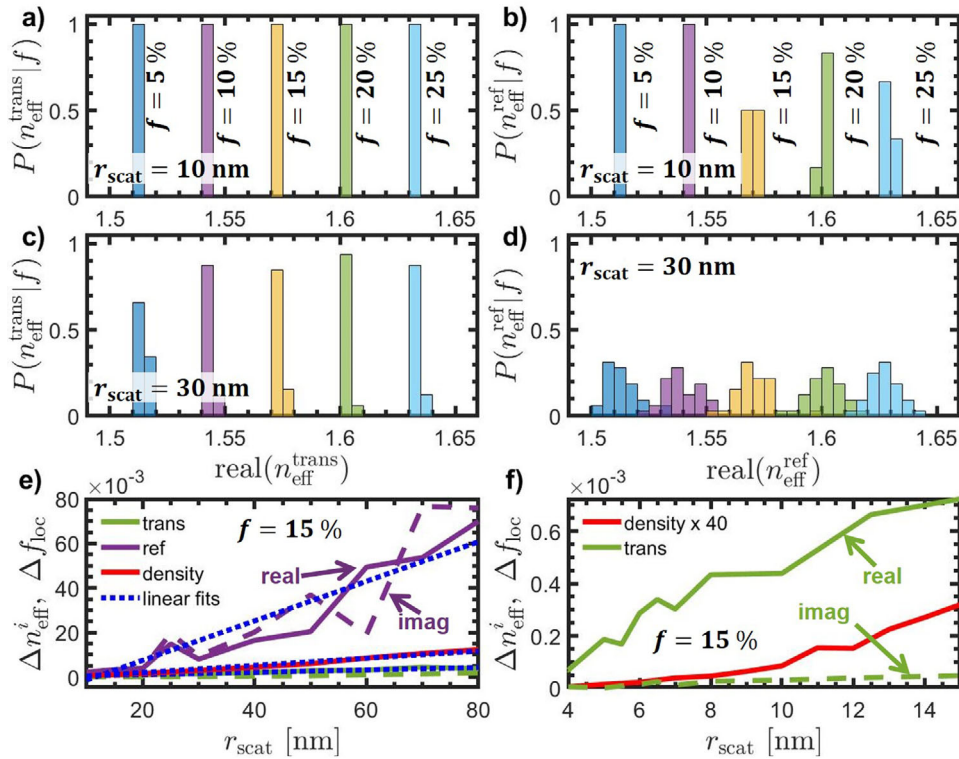
particles,[53–56] since such large-scale simulations were previously not possible.

## 5. The Transition from Homogeneous to Heterogeneous Materials

Building on the finding that we are able to study bulk optical materials at the single scatterer level, we can now fully investigate the transition from homogeneous to heterogeneous optical materials. In this section, we show that, across this transition, the concept of an effective refractive index successively breaks down on different levels. Across this transition, the concept of an effective refractive index consequently loses most of its physical meaning. We systematically analyze the different levels throughout on which this breakdown occurs in the following subsections. Furthermore, we highlight that this has direct implications for the design of novel optical nanocomposites. For this analysis, we mainly focus on radii between $r_{scat} = 10$ nm and $r_{scat} = 80$ nm. As we show below, this is the range within which the most drastic changes occur for a wavelength of $\lambda_0 = 0.8$ μm. To ensure that we are well within the bulk regime for this range of radii (Figure 3 and Supporting Information), we keep the distributions' lengths and widths fixed at $l_{dist} = 20r_{scat}$ and $w_{dist} = 6\omega_{beam}$, respectively. We chose a much larger width than the one required to achieve convergence for small particles (Figure 3) to compensate for the increase of $l_{dist}$ with increasing radius. Furthermore, we chose a length of $l_{dist} = 20r_{scat}$ since the effective refractive indices converge to well-defined values at this length also for radii above $r_{scat} = 10$ nm (see Supporting Information).

### 5.1. Refractive Index Fluctuations

Nowadays conventional optical materials have highly reproducible refractive indices.[57] In other words, all microstates within an ensemble that is defined by a certain set of macroscopic parameters are characterized by the same refractive index. In contrast, for heterogeneous materials, we expect that statistical fluctuations start to play a role. To investigate this relationship in detail, we generated different random particle distributions while keeping the parameters that describe the ensembles'

**ADVANCED
SCIENCE NEWS**
www.advancedsciencenews.com

**ADVANCED
THEORY AND
SIMULATIONS**
www.advtheorysimul.com

**Figure 4.** Probability for obtaining a certain value of a,c) real ($n_{\text{eff}}^{\text{trans}}$) and b,d) real ($n_{\text{eff}}^{\text{ref}}$) for particle radii of a,b) $r_{\text{scat}} = 10\,\text{nm}$ and c,d) $r_{\text{scat}} = 30\,\text{nm}$ at fixed volume fractions ($f$). The histograms for each volume fraction were obtained by generating different random particle distributions while keeping all macroscopic parameters ($f$, $w_{\text{dist}}$, $l_{\text{dist}}$, and $r_{\text{scat}}$) constant. e) Fluctuations of the effective refractive index ($\Delta n_{\text{eff}}^i$) as obtained from the standard deviation ($\Delta n_{\text{eff}}^i = \sigma(\{n_{\text{eff}}^i\})$) over $r_{\text{scat}}$ for $10\,\text{nm} \leq r_{\text{scat}} \leq 80\,\text{nm}$. The red line depicts the local density fluctuations of the particle distribution ($\Delta f_{\text{loc}} = \sigma(\{f_{\text{loc}}(\Delta V_i)\})$) within a cube with a width of $a_{\text{cube}} = \lambda_0 = 0.8\,\mu\text{m}$. The dotted blue lines visualize that both the refractive index and density fluctuations increase approximately linearly with $r_{\text{scat}}$. f) Fluctuations of the effective refractive index in transmission and the local density over $r_{\text{scat}}$ for $4\,\text{nm} \leq r_{\text{scat}} \leq 15\,\text{nm}$. The density fluctuations (red line) were scaled by a factor of 40.

macroscopic properties fixed. For each of these microstates, we then retrieved the effective refractive index using all measures described above. First, we did so for different volume fractions between $f = 5\%$ and $f = 25\%$, and two particle radii of $r_{\text{scat}} = 10\,\text{nm}$ as well as $r_{\text{scat}} = 30\,\text{nm}$. Using this procedure, we obtained the histograms in **Figure 4**a–d. These figures show that, at $r_{\text{scat}} = 10\,\text{nm}$, the effective refractive index obtained from the transmitted component ($n_{\text{eff}}^{\text{trans}}$; see Figure 4a) is well-defined, whereas the values obtained from the reflected component exhibit small fluctuations ($n_{\text{eff}}^{\text{ref}}$; see Figure 4b). This shows that, already at a radius of $r_{\text{scat}} = 10\,\text{nm}$, which corresponds to a ratio of $\frac{d_{\text{scat}}}{\lambda} = \frac{1}{40}$ ($d_{\text{scat}} = 2r_{\text{scat}}$), the effective refractive index is no longer solely defined by the macroscopic parameters $f$, $w_{\text{dist}}$, $l_{\text{dist}}$, and $r_{\text{scat}}$, but also depends on the specific particle positions of the microstate. In fact, this effect becomes more pronounced for a particle radius of $r_{\text{scat}} = 30\,\text{nm}$. This can be seen from Figure 4c,d, which demonstrate that, at this radius, the values obtained from the transmitted component exhibit small fluctuations (Figure 4d), whereas major fluctuations, which span a range of around 0.5 RU (RU: refractive index units), are observed in reflection (Figure 4d). This shows that, as a material transitions out of the homogeneous regime, the effective refractive index is increasingly no longer a well-defined property that fully quantifies a material's response.

To investigate the influence of $r_{\text{scat}}$ on the refractive index fluctuations systematically, we subsequently fixed the volume fraction at $f = 15\%$ and varied $r_{\text{scat}}$ between 10 and 80 nm. For each particle radius, we then quantified the refractive index fluctuations using the standard deviation ($\Delta n_{\text{eff}}^i(f = 0.15) = \sigma(\{n_{\text{eff}}^i(f = 0.15)\})$). Accordingly, Figure 4e depicts the fluctuations in both the real and imaginary parts of the refractive index. These data demonstrate that the fluctuations increase close to linearly with the particle radius. Moreover, Figure 4e confirms that the fluctuations are much larger in reflection than in transmission at all radii. The reasons for this are most likely twofold: first, directly comparing the fluctuations in the reflection ($\Delta|r|$) and transmission coefficients ($\Delta|t|$) reveals that they are of similar magnitude ($\Delta|r| \approx \Delta|t|$). Since the amplitude of the transmitted component is much larger than that of the reflected component ($|r| \ll \langle\Delta|t|\rangle$), this implies that the signal to noise ratio is much smaller in reflection. Second, in the Supporting Information, we show using alternative nanosphere placement procedures that the effective refractive index retrieved in reflection is very sensitive to the location of the first interface. This indicates that, to a certain degree, the reflected component is more sensitive to the configuration of the scatterer distribution's first interface. However, we emphasize that all scatterers within

**ADVANCED
SCIENCE NEWS**
www.advancedsciencenews.com

**ADVANCED
THEORY AND
SIMULATIONS**
www.advtheorysimul.com

the distribution contribute to the reflected beam.[5] The finding that the effective refractive indices obtained in transmission and reflection can deviate from each other shows that the effective refractive index not only depends on the specific configuration of the microstate, but that the same microstate can even be characterized by widely different effective refractive indices, depending on the measure that is used (e.g., transmission or reflection). To gain insight into the physical mechanism that causes these fluctuations, we determined the distributions' density fluctuations on the scale of the wavelength. For this purpose, we used a cube with a length of $a_{cube} = \lambda_0$ and scanned this cube through the particle distributions. For each position $(r_j)$, we then determined the local volume fraction within the cube $(f_{loc}(r_j))$ by precisely calculating the partial volume of each nanosphere that is located within the cube (blue parts of the spheres in Figure 2b). This allows us to quantify the density fluctuations as the standard deviation of all local volume fractions $(\Delta f_{loc} = \sigma(\{f_{loc}(r_j)\}))$. The results of this analysis in Figure 4e, show that, for radii between $r_{scat} = 10\,nm$ and $r_{scat} = 80\,nm$, the density fluctuations also increase close to linearly. This suggests that density fluctuations are one of the key drivers behind the fluctuations of the effective refractive index.

Finally, the finding that the effective refractive index underlies strong statistical fluctuations outside the homogenous regime, also has direct implications for the design of optical nanocomposites. This is because materials in todays optical systems must have highly accurate and reproducible refractive indices (beyond the 4th digit).[57] Therefore, nanocomposites are only suitable for such applications if the refractive index fluctuations are suppressed. To investigate at what particle sizes this requirement can be fulfilled, we performed another series of simulations in which we included radii below $r_{scat} = 10\,nm$. For this analysis, we fixed the distributions' lengths and widths at the values that were required to achieve convergence for small particles ($l_{dist} = 20r_{scat}$ and $w_{dist} = 3\omega_{beam}$; see Figure 3). The data obtained from this series of simulations is depicted in Figure 4f. This figure shows that the refractive index fluctuations increase with increasing radii even for $r_{scat} < 10\,nm$. Specifically, a radius of $r_{scat} = 4\,nm$, which corresponds to a particle size $(d_{scat} = 2r_{scat})$ of $\frac{d_{scat}}{\lambda_0} = \frac{1}{100}$ is required to reduce the fluctuations in real $(n_{eff}^{trans})$ below $10^{-5}$. In fact, the red line in Figure 4f demonstrates that this size is also the threshold at which the density fluctuations become negligible. This demonstrates that the particle sizes in nanocomposites for optical systems should ideally be below $\frac{d_{scat}}{\lambda_0} = \frac{1}{100}$ to eliminate the fluctuations in the effective refractive index.
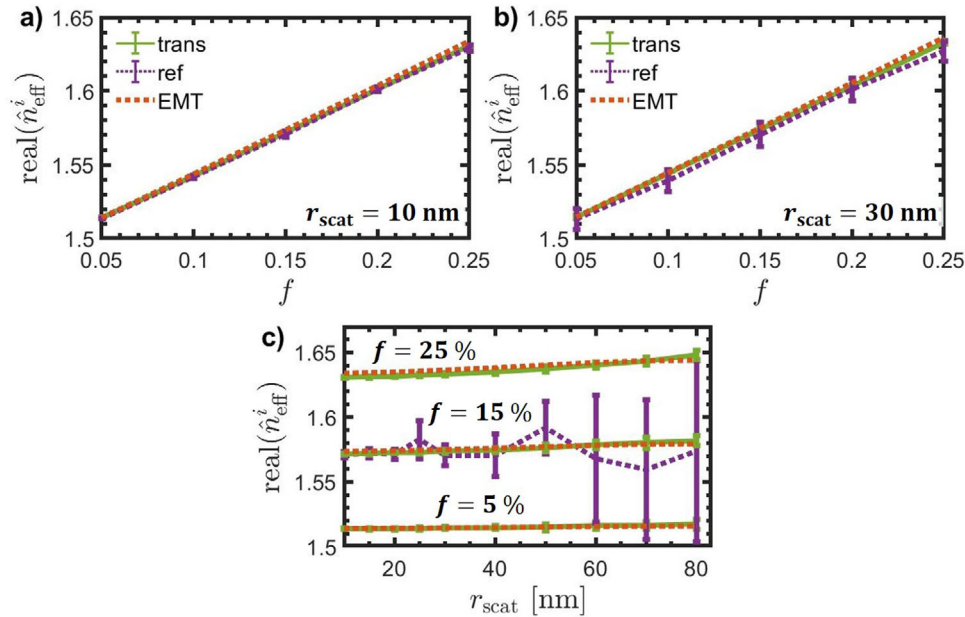
## 5.2. Ensemble Averages: The Real Part of the Effective Refractive Index

In the previous section, we have shown that outside the homogeneous regime, different microstates can be characterized by widely different effective refractive indices. Therefore, it is necessary to distinguish between a specific microstate and the ensemble average that is obtained by averaging over a sufficiently large number of microstates. Just like the laws of thermodynamics, effective medium theories cannot account for statistical fluctuations. However, a key question is whether effective medium theories can predict the ensemble average and are hence accurate

tools for the design of novel dispersion-engineered materials. In this subsection, we address these questions for the real part of the effective refractive index. We investigate the imaginary part in the following subsection. In all following figures, we include error bars to visualize the refractive index fluctuations ($\Delta n_{eff}^i$).

As the first step, **Figure 5**a visualizes that at $r_{scat} = 10\,nm$, the ensemble averages obtained in both transmission and reflection are identical at all volume fractions between $f = 5\%$ and $f = 25\%$ (Figure 5a). However, this is no longer the case at a radius of $r_{scat} = 30\,nm$ (Figure 5b). This shows that, for larger scatterers, even the ensemble average depends on the measurement modality. Finally, it is evident from Figure 5a, b that the EMT predicts the ensemble averages for the transmitted component with good accuracy, but slightly overestimates real $(\hat{n}_{eff}^{trans})$ at large volume fractions. Below we discuss that this can possibly be attributed to the fact that the distributions' interfaces are not well-defined for larger scatterers.

As the second step, to again investigate the influence of the particle radius systematically, we chose three different volume fractions ($f = 5\%$, $f = 15\%$, and $f = 25\%$) and varied $r_{scat}$ between 10 and 80 nm. The results of this series of simulations are depicted in Figure 5c. This figure confirms that the EMT predicts the real part of the effective refractive index obtained in transmission with good accuracy. This holds for all radii. We only notice a slightly impaired accuracy at the highest volume fraction of $f = 25\%$. In addition, we show in the Supporting Information that the results obtained from the equation for metamaterials almost perfectly match the ones obtained in transmission even for the largest radius of $r_{scat} = 80\,nm$. This shows that the scatterers' magnetic dipole response is negligible. Therefore, the finding that real $(\hat{n}_{eff}^{trans})$ starts to exhibit a size dependence for larger radii (Figure 5c), can be attributed to the electric dipole resonance. Finally, Figure 5c also shows that, in contrast to transmission, major fluctuations are again present in reflection. This can be seen from the purple line, which demonstrates that the error bars span a range that exceeds 0.1 RU. In addition, even the ensemble averages fluctuate heavily around the EMT prediction for larger radii. Since the effective refractive indices obtained in reflection for the other volume fractions also fluctuate heavily, the remaining data is provided in the Supporting Information to ensure the clarity of Figure 5c. The strong fluctuations show that, in reflection, the concept of an effective refractive index losses its applicability for radii exceeding $r_{scat} = 30\,nm$. In this regime, an effective refractive index can consequently only be used to describe the transmitted component. For this component, the EMT's prediction must then be understood as an ensemble average that is obtained by averaging over a large number of microstates, or alternatively, a large volume. If the EMT's prediction is treated in this manner, it can generally predict the real part of the effective refractive index with good accuracy (Figure 5). This holds true even at high volume fractions, for which multiple scattering plays a major role. Since accurately tailoring the real part of the effective refractive index is the key design goal for novel dispersion-engineered materials, this shows that the EMT is an accurate tool for such purposes. In fact, in Section 5.4, we demonstrate that the EMT's accuracy can be even further improved by compensating for the fact that the interfaces are not well-defined for larger scatterers.

**ADVANCED
SCIENCE NEWS**
www.advancedsciencenews.com

**ADVANCED
THEORY AND
SIMULATIONS**
www.advtheorysimul.com

**Figure 5.** Ensemble average of the real part of the effective refractive index (real $(\hat{n}_{\text{eff}}^i)$) as a function of the volume fraction ($f$) for radii of a) $r_{\text{scat}} = 10\,\text{nm}$ and b) $r_{\text{scat}} = 30\,\text{nm}$. All plots include the data obtained from transmission, reflection, and the EMT ($i \in \{\text{trans, ref, EMT}\}$). The ensemble averages were obtained by averaging across different microstates (random distributions) and the errorbars were determined as the corresponding standard deviations ($\Delta n_{\text{eff}}^i = \sigma(\{n_{\text{eff}}^i\})$). c) Ensemble average of the real part of the effective refractive index (real $(\hat{n}_{\text{eff}}^i)$) as a function of the nanosphere radius ($r_{\text{scat}}$) at volume fractions of $f = 5\%$, $f = 15\%$, and $f = 25\%$ ($i \in \{\text{trans, ref, EMT}\}$). For the reflected component only the data for $f = 15\%$ is included to improve clarity. The data for the other volume fractions is included in the Supporting Information.

### 5.3. The Imaginary Part of the Effective Refractive Index: The Influence of Incoherent Scattering
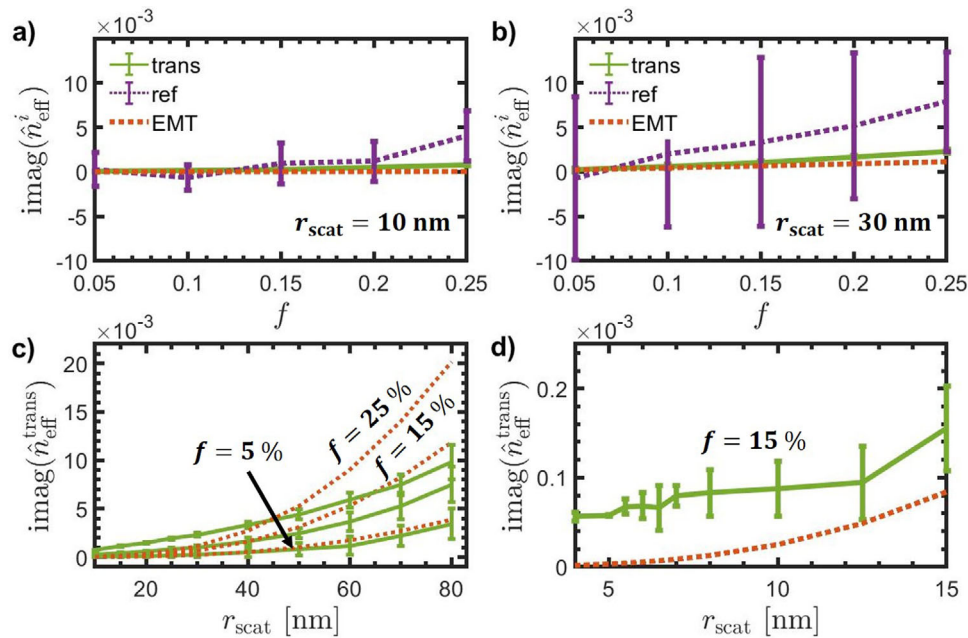
In this subsection, we analyze the imaginary part of the effective refractive index. This allows us to quantify the overall attenuation a beam of light experiences. Attenuation is a key issue for materials outside the homogeneous regime, since incoherent scattering plays a major role as a loss mechanism for such materials.[17,24] We use the term incoherent scattering[58,59] because, on the microscopic level, all electromagnetic charges scatter light. Therefore, it is necessary to distinguish the coherent field, which is the propagating beam itself, and the incoherent field, which is made up by the radiation that is incoherently scattered out of the beam.[24,58,59] Within the concept of an effective refractive index, incoherent scattering manifests itself as an increase of the imaginary part of the effective refractive index. This is because incoherent scattering attenuates the coherent beam by scattering a portion of its energy in other directions.[17,24] The onset of incoherent scattering consequently also restricts the applicability of the effective refractive index, because it distorts a beam of light (Figure 1) and imag $(\hat{n}_{\text{eff}})$ can hence no longer be used to determine the absorption rate and the appearance of the material.[17] Note that the imaginary part of the effective refractive index directly determines the attenuation coefficient ($\gamma$) in the Beer–Lambert law ($I(z) = I(0)\exp(\gamma z)$, where $I$ is the intensity and $z$ the propagation distance) according to $\gamma = \frac{4\pi}{\lambda}\text{imag}\,(\hat{n}_{\text{eff}})$.[17] This attenuation coefficient then accounts for both incoherent scattering and absorption. In the absence of absorption, it can hence be used to directly determine a mean free path of the photons within the scatterer distribution. This mean free path then describes the

average distance photons can cover, while constantly undergoing coherent scattering, until they are incoherently scattered.

**Figure 6**a,b depicts the ensemble averages for the imaginary part of the effective refractive index as a function of the volume fraction for $r_{\text{scat}} = 10\,\text{nm}$ (Figure 6a) and $r_{\text{scat}} = 30\,\text{nm}$ (Figure 6b). These figures show that, in transmission, the imaginary part of the effective refractive index depends only weakly on the volume fraction. Furthermore, for this component, the imaginary part of the effective refractive index (imag $(\hat{n}_{\text{eff}}^{\text{trans}})$) agrees well with the EMT for small volume fractions, but the EMT slightly overestimates the attenuation at larger volume fractions. In contrast, in reflection, the imaginary part increases drastically with the volume fraction, fluctuates heavily, and does not agree well with the EMT. In fact, for this component, the imaginary part (imag $(\hat{n}_{\text{eff}}^{\text{ref}})$) can even become negative for some configurations. This shows that, in these cases, the plane wave propagating in the normal directions is amplified at the expense of plane waves with oblique incidence angles. In transmission, this effect is less dominant because the overall amplitude of the signal is much larger ($|t| \gg |r|$).

To again investigate the influence of the radius systematically, Figure 6c depicts imag $(\hat{n}_{\text{eff}}^{\text{trans}})$ as a function of the radius for three different volume fractions ($f = 5\%$, $f = 15\%$, and $f = 25\%$). The data for the reflected component is shown in the Supporting Information. Figure 6c demonstrates that, at small radii and volume fractions, the EMT predicts imag $(\hat{n}_{\text{eff}}^{\text{trans}})$ with decent accuracy, but looses its accuracy if either parameter is increased (Figure 6c). This shows that statistical effects play a major role for large volume fractions and radii. This is because the EMT can only account for the influence of the particle size, but not

**ADVANCED
SCIENCE NEWS**
www.advancedsciencenews.com

**ADVANCED
THEORY AND
SIMULATIONS**
www.advtheorysimul.com

**Figure 6.** Ensemble average of the imaginary part of the effective refractive index (imag $(\hat{n}^i_{\text{eff}})$) as a function of the volume fraction ($f$) for radii of a) $r_{\text{scat}} = 10$ nm and b) $r_{\text{scat}} = 30$ nm. All plots include the data obtained from transmission, reflection, and the EMT ($i \in \{\text{trans}, \text{ref}, \text{EMT}\}$). The ensemble averages were obtained by averaging across different microstates (random distributions) and the errorbars were determined as the corresponding standard deviations ($\Delta n^i_{\text{eff}} = \sigma(\{n^i_{\text{eff}}\})$). c) Ensemble average of the imaginary part of the effective refractive index in transmission (imag $(\hat{n}^{\text{trans}}_{\text{eff}})$) as a function of the nanosphere radius ($r_{\text{scat}}$) at volume fractions of $f = 5\%$, $f = 15\%$, and $f = 25\%$ ($i \in \{\text{trans}, \text{ref}, \text{EMT}\}$). For the sake of clarity, the missing data for the reflected component is shown in the Supporting Information because of its strong fluctuations. d) imag $(\hat{n}^{\text{trans}}_{\text{eff}})$ as a function of $r_{\text{scat}}$ at a volume fraction of $f = 15\%$ for $4\,\text{nm} \leq r_{\text{scat}} \leq 15\,\text{nm}$.

for statistical deviations from perfect random distributions. Our results consequently also show that both the particle size itself as well as statistical variances, critically determine the overall amount of incoherent scattering. Furthermore, we show in the Supporting Information that incoherent scattering also causes the effective refractive indices to depend on the particle distribution's width, even if the distribution is a factor of 10 wider than the beam waist ($\omega_{\text{beam}}$). This is because light that is scattered out of the forward and backward directions leads to the emergence of long-ranged modes that propagate along the entire width of the distribution and hence affects the distribution's properties. Since, for homogeneous materials, the refractive index in the bulk region is independent of the size, this width dependence adds another key level on which the concept of an effective refractive index breaks down outside the homogeneous regime.

Finally, in an imaging system, incoherent scattering leads to stray light and hence a loss of contrast.[17] Therefore, it is essential to minimize incoherent scattering by using sufficiently small particle sizes ($d_{\text{scat}}$). To investigate what particle sizes are required to fulfill this requirement, we again used our data for smaller radii from Section 5.1. Accordingly, Figure 6d depicts imag $(\hat{n}^i_{\text{eff}})$ for radii between $4\,\text{nm} \leq r_{\text{scat}} \leq 15\,\text{nm}$. This figure shows that radii significantly below $r_{\text{scat}} = 10\,\text{nm}$ are required to minimize the amount of incoherent scattering. In fact, in agreement with the EMT, imag $(\hat{n}^{\text{trans}}_{\text{eff}})$ appears to converge to its minimum around $r_{\text{scat}} = 4\,\text{nm}$. It appears likely that this minimum corresponds to the resolution limit of our numerical procedure, which could also explain the systematic shift between the EMT and our nu-

merical data. This shows that particle sizes around or ideally below $\frac{d_{\text{scat}}}{\lambda_0} = \frac{1}{100}$ are required to minimize incoherent scattering. To cover the entire visible spectrum ($400\,\text{nm} \leq \lambda \leq 800\,\text{nm}$), the particle size must consequently be within the range in which its properties become size-dependent. Since this range corresponds to the quantum-dot regime,[60,61] this opens up new possibilities for tailoring the refractive index and its dispersion. This is because any material's refractive index is critically determined by the resonances, that is, the absorption lines, within the system.[57] Tailoring the absorption lines of quantum dots by adjusting their size or surface[62–64] could hence provide a powerful new degree of freedom for tailoring the refractive index and its dispersion that has never been explored.

### 5.4. Effective Interfaces

Another fundamental consequence of increasing the size of the particles is that the materials' interfaces are no longer well-defined. To visualize this directly, **Figure 7**a depicts the local volume fraction ($f_{\text{loc}}$) as a function of the spatial coordinate $z$ for a particle radius of $r_{\text{scat}} = 30\,\text{nm}$. It is evident that the volume fraction increases gradually from zero to its bulk value within a distance that is equal to the particles' size ($d_{\text{scat}} = 2r_{\text{scat}} = 60\,\text{nm}$). While this is the case for all materials, this effect does not play a role for conventional materials whose building blocks are atoms or small molecules. However, all equations that we use to determine the effective refractive index depend explicitly on
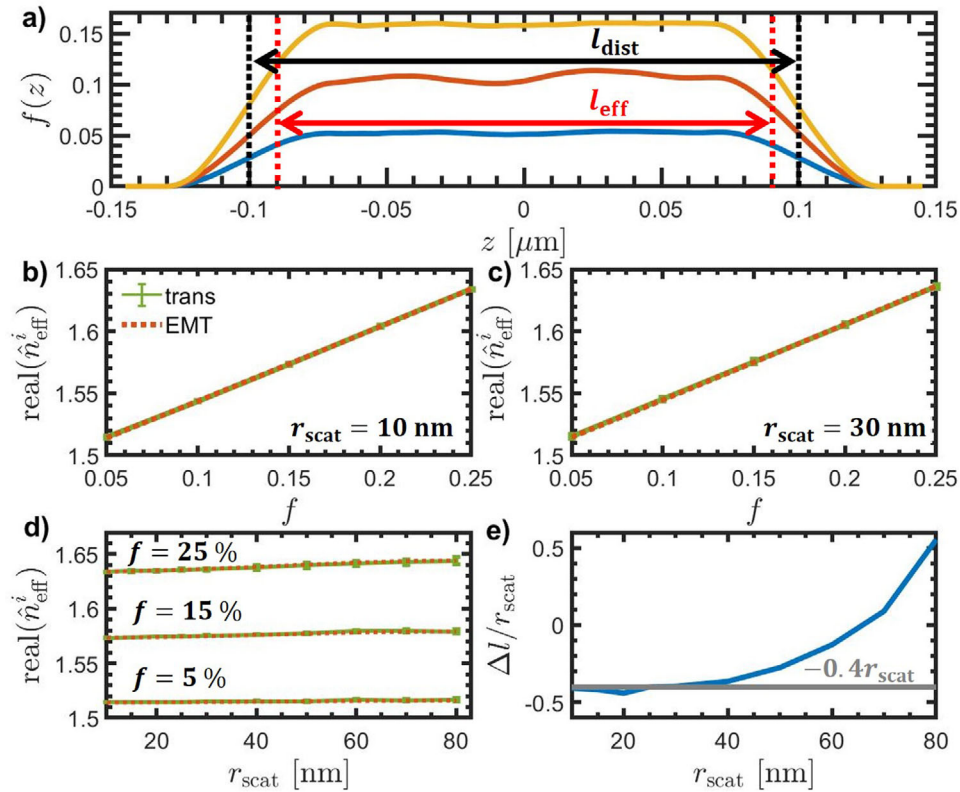
**Figure 7.** a) Local volume fraction ($f_{loc}$) as a function of the spatial coordinate $z$ to show that the interfaces are not well-defined for larger particles (here $r_{scat} = 30$ nm). We determine the effective length $l_{eff}$ by optimizing it for the best agreement of real ($\hat{n}_{eff}^{trans}$) with the EMT-prediction simultaneously for all volume fractions at each radius ($r_{scat}$). b,c) Ensemble averages for the real part of the effective refractive index (real ($\hat{n}_{eff}^i$)) using effective lengths for b) $r_{scat} = 10$ nm and c) $r_{scat} = 30$ nm. d) Analogous plot as a function of the particle radius ($r_{scat}$) at a volume fractions of $f = 5\%$, $f = 15\%$ and $f = 25\%$. The effective interface was determined for each radius individually. The data for the imaginary part is depicted in the Supporting Information. e) Difference $\Delta l = (l_{dist} - l_{eff})$ between the length of the particle distribution ($l_{dist}$) and the effective length ($l_{eff}$) as a fraction of the radius ($r_{scat}$).

the length of the particle distribution ($l_{dist}$; see Equation (3)). Therefore, the question arises whether the fact that this length no longer is well-defined for larger scatterers can compensate for the finding that the EMT systematically overestimates the real part of the effective refractive index at larger volume fractions (Figure 5). To investigate whether this is possible, we introduced the effective length ($l_{eff}$) as a free parameter and optimized it for the best agreement of real ($\hat{n}_{eff}^{trans}$) with the EMT. Since an effective length should depend only on the particle radius, we performed this optimization for all volume fractions ($5\% \leq f \leq 25\%$) simultaneously. First, we did so for two fixed radii ($r_{scat} = 10$ nm and $r_{scat} = 30$ nm). For both radii, we thus obtained an effective length that is $0.4r_{scat}$ shorter than $l_{dist}$. As shown in Figure 7b,c, this yielded a perfect agreement between the EMT's prediction and the numerical results. In the Supporting Information, we additionally demonstrate that the level of agreement between imag ($\hat{n}_{eff}^{trans}$) and the EMT is also maintained for both radii even though it was not included in our procedure for determining the effective length. In addition, Figure 7d shows that the concept of an effective length also allows us to achieve an essentially perfect agreement between the EMT and real ($\hat{n}_{eff}^{trans}$) for all other radii between $r_{scat} = 10$ nm and $r_{scat} = 80$ nm. To visualize the influence of the radii on the effective length, Figure 7e depicts the difference between $l_{dist}$ and $l_{eff}$ ($\Delta l = l_{dist} - l_{eff}$) as a function of the

particle radius $r_{inc}$. It is evident that for radii below $r_{scat} = 40$ nm, the effective length is always $0.4r_{scat}$ shorter than $l_{dist}$. In contrast, for larger particles, a continuous increase is seen. However, $\Delta l$ never exceeds the nanospheres' radius ($r_{scat}$). This suggests that an additional physical mechanism starts to influence the effective length for larger nanospheres. For example, it appears possible that the effective length can compensate the influence of the distributions' width that plays an increasing role for larger particles (see Supporting Information). However, even for these radii, combining the EMT with our concept of an effective length allows for a perfect match between the analytical and the numerical results. Finally, our discussion of the concept of effective interfaces illustrates that, outside the homogeneous regime, it is no longer possible to assign an effective refractive index to a fixed region in space. It is evident that instead the gradual increase of the local volume fraction plays an increasingly important role.

## 6. Conclusion

Across a time span over several decades, numerical simulations have significantly advanced our understanding of light transport in heterogeneous media that contain large scatterers.[8–13] However, the regime in which a distribution of scatterers acts as a bulk homogeneous medium and the transition to heterogeneous

**ADVANCED
SCIENCE NEWS**

www.advancedsciencenews.com

**ADVANCED
THEORY AND
SIMULATIONS**

www.advtheorysimul.com

materials have never been investigated using such approaches. Therefore, we still have a limited understanding of these regimes. In this paper, we have demonstrated that it is now possible to numerically model materials in the homogeneous regime at the single scatterer level and leverage this possibility to guide the design of novel materials. To this end, we have first introduced a procedure that allows for obtaining reliable refractive index values from numerical simulations of the full multibody scattering problem that includes hundreds of thousands of individual scatterers. Using this approach we have then shown that an effective refractive index is only a well-defined concept for scatterer sizes ($d_{scat}$) up to $d_{scat} = \frac{\lambda}{100}$. For larger scatterers, a successive transition into the heterogeneous regime occurs, which leads to the breakdown of the concept of an effective refractive index on multiple levels: First, the effective refractive index begins to exhibit statistical fluctuations that depend on the specific configuration of the microstate. Second, a given microstate can be characterized by widely different effective refractive indices depending on the measurement modality that is used (e.g., reflection or transmission). Therefore, the concept of an effective refractive index no longer fully quantifies the optical response. Third, a beam of light is distorted because of incoherent scattering. This also causes the effective refractive index to depend on the distributions' widths. Fourth, the distributions interfaces are no longer well defined and it is hence not possible to assign an effective refractive index to a fixed region in space. Throughout this paper, we have discussed that these fundamental findings have direct practical implications for the design of novel optical nanocomposite materials. This is because modern optical systems require materials that are characterized by highly reproducible refractive indices and negligible amounts of incoherent scattering. Therefore, our results show that nanocomposites for such applications must contain nanoparticles that are ideally smaller than $d_{scat} = \frac{\lambda}{100}$. Furthermore, we have demonstrated that the Maxwell–Garnett–Mie effective medium theory can predict the real part of the effective refractive index with high accuracy. It is consequently an ideal tool for the design of novel dispersion-engineered materials.[19]

In this paper, we have focused on random nanocomposites that contain nanospheres at volume fractions below $f = 30\%$ because this range is experimentally accessible[43–49] and offers an unprecedented control of the magnitude and dispersion of the effective refractive index.[19] However, our approach can be readily generalized: First, to other types of scatterers, including atoms, molecules,[22] as well as nanoparticles with other shapes[8,29–31,65,66] and, second, also to other kinds of particle distributions. Specifically, both random packings[13,67–70] as well as the transition regime between ordered and disordered packings[71–74] exhibit a fascinating complexity. In the future, using our approach to investigate such packings at the threshold between the homogeneous and heterogeneous regimes will allow us to obtain a much deeper understanding of optical materials. Just like for the materials investigated in this paper, such investigations will likely also be able to guide the design of novel materials. In fact, optical 3D nanocomposites are a highly diverse material class that can exhibit a wide range of novel properties of which we are just beginning to develop a deeper understanding.[75–80] As for the design of dispersion-engineered nanocomposites, the finding that nanoparticles' sizes must be below $d_{scat} = \frac{\lambda}{100}$ opens up new possibilities for tailoring the effective refractive index

that have never been explored. This is because, for applications that span the entire visible spectrum, these sizes are within the quantum dot regime, in which the nanoparticles' electronic transitions can be tailored by varying their size and surface.[62–64] Doing so can likely extend the dispersion-engineering capabilities of nanocomposites[16] even further.

## Supporting Information

Supporting Information is available from the Wiley Online Library or from the author.

## Conflict of Interest

The authors declare no conflict of interest.

## Keywords

[1] J. D. Jackson, *Classical Electrodynamics*, John Wiley & Sons, New York **2012**.

[2] C. F. Bohren, D. R. Huffman, *Absorption and Scattering of Light By Small Particles*, John Wiley & Sons, New York **2008**.

[3] H. Gross, W. Singer, M. Totzeck, F. Blechinger, B. Achtner, *Handbook of Optical Systems*, Vol. 1, Wiley-VCH, Berlin **2005**.

[4] D. Aspnes, *Am. J. Phys.* **1982**, *50*, 704.

[5] H. Fearn, D. F. James, P. W. Milonni, *Am. J. Phys.* **1996**, *64*, 986.

[6] V. C. Ballenegger, T. Weber, *Am. J. Phys.* **1999**, *67*, 599.

[7] G. Russakoff, *Am. J. Phys.* **1970**, *38*, 1188.

[8] M. I. Mishchenko, L. Liu, D. W. Mackowski, B. Cairns, G. Videen, *Opt. Express* **2007**, *15*, 2822.

[9] M. I. Mishchenko, L. D. Travis, *Opt. Commun.* **1994**, *109*, 16.

[10] M. I. Mishchenko, L. D. Travis, A. A. Lacis, *Scattering, Absorption, and Emission of Light by Small Particles*, Cambridge University Press, Cambridge, MA **2002**.

[11] A. Macke, M. I. Mishchenko, K. Muinonen, B. E. Carlson, *Opt. Lett.* **1995**, *20*, 1934.

**ADVANCED**
**SCIENCE NEWS**

www.advancedsciencenews.com

**ADVANCED**
**THEORY AND**
**SIMULATIONS**

www.advtheorysimul.com

[12] Z. Cui, Y. Han, Q. Xu, *J. Opt. Soc. Am. A* **2011**, *28*, 2200.

[13] L. Pattelli, A. Egel, U. Lemmer, D. S. Wiersma, *Optica* **2018**, *5*, 1037.

[14] D. W. Mackowski, M. I. Mishchenko, *J. Opt. Soc. Am. A* **1996**, *13*, 2266.

[15] J. Bertolotti, K. Vynck, D. S. Wiersma, *Phys. Rev. Lett.* **2010**, *105*, 163902.

[16] D. Werdehausen, S. Burger, I. Staude, T. Pertsch, M. Decker, *Optica* **2019**, *6*, 1031.

[17] D. Werdehausen, I. Staude, S. Burger, J. Petschulat, T. Scharf, T. Pertsch, M. Decker, *Opt. Mater. Express* **2018**, *8*, 3456.

[18] D. Werdehausen, T. Scharf, J. Petschulat, S. Burger, T. Pertsch, I. Staude, M. Decker, In, *Proc. SPIE 10745, Current Developments in Lens Design and Optical Engineering XIX* (Eds: R. B. Johnson, V. N. Mahajan, S. Thibault), SPIE, Bellingham, WA **2018**, p. 107450H.

[19] D. Werdehausen, S. Burger, I. Staude, T. Pertsch, M. Decker, *Opt. Express* **2020**, *28*, 6452.

[20] D. Werdehausen, S. Burger, I. Staude, T. Pertsch, M. Decker, In *Optical Design and Fabrication 2019 (Freeform, OFT)*, OSA Technical Digest. Optical Society of America, Washington, DC **2019**, p. OT2A.2. http://www.osapublishing.org/abstract.cfm?URI=OFT-2019-OT2A.2

[21] D. Werdehausen, S. Burger, I. Staude, T. Pertsch, M. Decker, *J. Opt.* **2020**, *22*, 065607.

[22] I. Fernandez-Corbaton, D. Beutel, C. Rockstuhl, A. Pausch, W. Klopper, *ChemPhysChem* **2020**, *21*, 878.

[23] V. A. Markel, *J. Opt. Soc. Am. A* **2016**, *33*, 1244.

[24] C. F. Bohren, *J. Atmos. Sci.* **1986**, *43*, 468.

[25] P. Mallet, C.-A. Guérin, A. Sentenac, *Phys. Rev. B* **2005**, *72*, 014205.

[26] A. Egel, L. Pattelli, G. Mazzamuto, D. S. Wiersma, U. Lemmer, *J. Quant. Spectrosc. Radiat. Transfer* **2017**, *199*, 103.

[27] K. Weber, D. Werdehausen, P. König, S. Thiele, M. Schmid, M. Decker, P. W. De Oliveira, A. Herkommer, H. Giessen, *Opt. Mater. Express* **2020**, *10*, 2345.

[28] A. H. Sihvola, *Electromagnetic Mixing Formulas and Applications, 47*, Institute of Engineering and Technology, Lucknow, India **1999**.

[29] X. G. Santiago, M. Hammerschmidt, S. Burger, C. Rockstuhl, I. Fernandez-Corbaton, L. Zschiedrich, *Phys. Rev. B* **2019**, *99*, 045406.

[30] D. Theobald, A. Egel, G. Gomard, U. Lemmer, *Phys. Rev. B* **2017**, *96*, 033822.

[31] M. I. Mishchenko, L. D. Travis, A. Macke, *Appl. Opt.* **1996**, *35*, 4927.

[32] J. Venermo, A. Sihvola, *J. Electrost.* **2005**, *63*, 101.

[33] A. H. Sihvola, J. A. Kong, *IEEE Trans. Geosci. Remote Sens.* **1988**, *26*, 420.

[34] T. Wu, A. Baron, P. Lalanne, K. Vynck, *Phys. Rev. A* **2020**, *101*, 011803.

[35] M. Bertrand, A. Devilez, J.-P. Hugonin, P. Lalanne, K. Vynck, *J. Opt. Soc. Am. A* **2020**, *37*, 70.

[36] W. T. Doyle, *Phys. Rev. B* **1989**, *39*, 9852.

[37] G. Mie, *Ann. Phys.* **1908**, *330*, 377.

[38] B. Freireich, M. Kodam, C. Wassgren, *AIChE J.* **2010**, *56*, 3036.

[39] F. Chen, P. R. Bakic, A. D. A. Maidment, S. T. Jensen, X. Shi, D. D. Pokrajac, *IEEE Trans. Med. Imaging* **2015**, *34*, 2146.

[40] A. Rahbari, R. Hens, I. K. Nikolaidis, A. Poursaeidesfahani, M. Ramdin, I. G. Economou, O. A. Moultos, D. Dubbeldam, T. J. H. Vlugt, *Mol. Phys.* **2018**, *116*, 3331.

[41] M. Decker, I. Staude, *J. Opt.* **2016**, *18*, 103001.

[42] N. Sultanova, S. Kasarova, I. Nikolov, *Acta Phys. Pol., A* **2009**, *116*, 585.

[43] P. Tao, Y. Li, A. Rungta, A. Viswanath, J. Gao, B. C. Benicewicz, R. W. Siegel, L. S. Schadler, *J. Mater. Chem.* **2011**, *21*, 18623.

[44] J. L. H. Chau, Y.-M. Lin, A.-K. Li, W.-F. Su, K.-S. Chang, S. L.-C. Hsu, T.-L. Li, *Mater. Lett.* **2007**, *61*, 2908.

[45] S. Lee, H.-J. Shin, S.-M. Yoon, D. K. Yi, J.-Y. Choi, U. Paik, *J. Mater. Chem.* **2008**, *18*, 1751.

[46] C. Lü, Z. Cui, Z. Li, B. Yang, J. Shen, *J. Mater. Chem.* **2003**, *13*, 526.

[47] C. Lü, Z. Cui, Y. Wang, Z. Li, C. Guan, B. Yang, J. Shen, *J. Mater. Chem.* **2003**, *13*, 2189.

[48] C. Lü, B. Yang, *J. Mater. Chem.* **2009**, *19*, 2884.

[49] R. J. Nussbaumer, W. R. Caseri, P. Smith, T. Tervoort, *Macromol. Mater. Eng.* **2003**, *288*, 44.

[50] D. R. Smith, S. Schultz, P. Markoš, C. M. Soukoulis, *Phys. Rev. B* **2002**, *65*, 19.

[51] C. Rockstuhl, T. Zentgraf, H. Guo, N. Liu, C. Etrich, I. Loa, K. Syassen, J. Kuhl, F. Lederer, H. Giessen, *Appl. Phys. B* **2006**, *84*, 219.

[52] E. Ospadov, J. Tao, V. N. Staroverov, J. P. Perdew, *Proc. Natl. Acad. Sci.* **2018**, *115*, E11578.

[53] M. Albooyeh, D. Morits, S. A. Tretyakov, *Phys. Rev. B* **2012**, *85*, 20.

[54] M. Dupré, L. Hsu, B. Kanté, *Sci. Rep.* **2018**, *8*, 1.

[55] C. Etrich, S. Fahr, M. Hedayati, F. Faupel, M. Elbahri, C. Rockstuhl, *Materials* **2014**, *7*, 727.

[56] C. Helgert, C. Rockstuhl, C. Etrich, C. Menzel, E.-B. Kley, A. Tünnermann, F. Lederer, T. Pertsch, *Phys. Rev. B* **2009**, *79*, 23.

[57] P. Hartmann, R. Jedamzik, S. Reichel, B. Schreder, *Appl. Opt.* **2010**, *49*, D157.

[58] L. L. Foldy, *Phys. Rev.* **1945**, *67*, 107.

[59] M. Lax, *Rev. Mod. Phys.* **1951**, *23*, 287.

[60] Y. Wang, N. Herron, *J. Phys. Chem.* **1991**, *95*, 525.

[61] N. Satoh, T. Nakashima, K. Kamikura, K. Yamamoto, *Nat. Nanotechnol.* **2008**, *3*, 106.

[62] M. Soreni-Harari, N. Yaacobi-Gross, D. Steiner, A. Aharoni, U. Banin, O. Millo, N. Tessler, *Nano Lett.* **2008**, *8*, 678.

[63] S. Chandra, S. H. Pathan, S. Mitra, B. H. Modha, A. Goswami, P. Pramanik, *RSC Adv.* **2012**, *2*, 3602.

[64] J. M. Garcia, T. Mankad, P. O. Holtz, P. J. Wellman, P. M. Petroff, *Appl. Phys. Lett.* **2020**, *72*, 3172.

[65] E. A. Muljarov, T. Weiss, *Opt. Lett.* **2018**, *43*, 1978.

[66] T. Weiss, E. A. Muljarov, *Phys. Rev. B* **2018**, *98*, 8.

[67] R. M. Ziff, S. Torquato, *J. Phys. A: Math. Theor.* **2017**, *50*, 085001.

[68] S. Torquato, *J. Chem. Phys.* **2018**, *149*, 020901.

[69] S. Atkinson, F. H. Stillinger, S. Torquato, *Proc. Natl. Acad. Sci. U. S. A.* **2014**, *111*, 18436.

[70] M. A. Klatt, S. Torquato, *Phys. Rev. E* **2018**, *97*, 012118.

[71] S. Torquato, F. H. Stillinger, *J. Phys. Chem. B* **2002**, *106*, 8354.

[72] M. V. Rybin, D. S. Filonov, K. B. Samusev, P. A. Belov, Y. S. Kivshar, M. F. Limonov, *Nat. Commun.* **2015**, *6*, 10102.

[73] M. Rechtsman, A. Szameit, F. Dreisow, M. Heinrich, R. Keil, S. Nolte, M. Segev, *Phys. Rev. Lett.* **2011**, *106*, 193904.

[74] L. Shi, Y. Zhang, B. Dong, T. Zhan, X. Liu, J. Zi, *Adv. Mater.* **2013**, *25*, 5314.

[75] S. Homaeigohar, M. Elbahri, *Adv. Opt. Mater.* **2018**, *7*, 1801101.

[76] M. K. Hedayati, M. Javaherirahim, B. Mozooni, R. Abdelaziz, A. Tavassolizadeh, V. S. K. Chakravadhanula, V. Zaporojtchenko, T. Strunkus, F. Faupel, M. Elbahri, *Adv. Mater.* **2011**, *23*, 5410.

[77] M. Gajc, H. B. Surma, D. A. Pawlak, *Sci. Rep.* **2018**, *8*, 13425.

[78] M. Gajc, H. B. Surma, A. Klos, K. Sadecka, K. Orlinski, A. E. Nikolaenko, K. Zdunek, D. A. Pawlak, *Adv. Funct. Mater.* **2013**, *23*, 3443.

[79] C. Sanchez, B. Lebeau, F. Chaput, J.-P. Boilot, *Adv. Mater.* **2003**, *15*, 1969.

[80] K. Wang, X. Zhang, I. M. Kislyakov, N. Dong, S. Zhang, G. Wang, J. Fan, X. Zou, J. Du, Y. Leng, Q. Zhao, K. Wu, J. Chen, S. M. Baesman, K. S. Liao, S. Maharjan, H. Zhang, L. Zhang, S. A. Curran, R. S. Oremland, W. J. Blau, J. Wang, *Nat. Commun.* **2019**, *10*, 3985.